

Estimation of OH in urban plume using TROPOMI inferred NO₂/ CO

Srijana Lama¹, Sander Houweling^{1,2}, K. Folkert Boersma^{3,4}, Ilse Aben^{2,1}, Hugo A. C. Denier van der Gon⁶, Maarten C. Krol^{3,7}

¹Vrije Universiteit, Department of Earth Sciences, Amsterdam, the Netherlands

5 ²SRON Netherlands Institute for Space Research, Leiden, the Netherlands

³Wageningen University, Meteorology and Air Quality Group, Wageningen, the Netherlands

⁴Royal Netherlands Meteorological Institute, R&D Satellite Observations, de Bilt, the Netherlands

⁶TNO, Department of Climate, Air and Sustainability, Princetonlaan, the Netherlands

⁷Institute for Marine and Atmospheric Research Utrecht, Utrecht University, Utrecht, the Netherlands

10 *Correspondence to:* Srijana Lama (s.lama@vu.nl, sreejanalama@gmail.com)

Abstract. A new method is presented to estimate urban hydroxyl radical (OH) concentrations using the downwind decay of the Tropospheric Monitoring Instrument (TROPOMI) derived nitrogen dioxide (NO₂)/carbon monoxide (CO) ratio combined with Weather Research Forecast (WRF) simulations. Seasonal OH concentrations, nitrogen oxides (NO_x) and CO emissions for summer (June to October, 2018) and winter (November, 2018 to March, 2019) are derived for Riyadh. WRF is able to spatially simulate NO₂ and CO urban plumes over Riyadh as observed by TROPOMI. However, WRF-simulated NO₂ plumes close to center of the city are overestimated by 25 % in summer and 40 to 50 % in winter compared to TROPOMI observations. WRF simulated CO plumes differ by 10 % with TROPOMI in both seasons. The differences between model and TROPOMI are used to optimize the OH concentration, NO_x and CO emissions iteratively using a least squares method. For summer, both the NO₂/CO ratio optimization and the XNO₂ optimization imply that the OH prior from the Copernicus Atmospheric Monitoring Service (CAMS) has to be increased by 32.03±4.0% . The OH estimations from the NO₂/CO ratio and the XNO₂ optimization differ by 10 %. Summer Emission Database for Global Atmospheric Research v4.3.2 (EDGAR) NO_x and CO emissions over Riyadh need to be increased by 42.1±8.7 % and 100.8±9.5%. For winter, the optimization method increases OH by ~52.0±5.3 %, while reducing NO_x emission by 15.45± 3.4% and doubling the CO emission. TROPOMI derived OH concentrations and pre-existing Exponentially Modified Gaussian function fit (EMG) method differ by 18 % in summer and 7.5 % in winter, confirming that urban OH concentrations can be reliably estimated using the TROPOMI-observed NO₂/CO ratio.

1 Introduction

The rapidly growing urbanization has led to an increase in the number of big cities globally. More than 55 % of the global population resides in cities and this fraction is projected to increase to 68% in 2050 (United Nations, 2018). The associated

30 rise in consumption of energy and materials leads to severe air pollution, threatening the health of the large urban population (Pascal et al., 2013; Sicard et al., 2021). Air pollution control measures and the application of cleaner technology have reduced the NO₂ concentrations in developed cities such as Los Angeles and Paris by 1.5 to 3.0 % yr⁻¹ between 1996 to 2017 (Georgoulas et al., 2019). The CO emission is reduced by 28.8 % to 60.7 % in these cities in the period 2000 to 2008 (Dekker et al., 2017). In developing cities such as Tehran and Baghdad, however, NO₂ concentrations have increased by 8.6 % yr⁻¹ and
35 16.9% yr⁻¹ between 1996 to 2017 (Georgoulas et al., 2019). The CO emission increased by 15% in New Delhi in the period 2000 to 2008 (Dekker et al., 2017). As a consequence, air pollution monitoring and mitigation in developing cities is becoming an increasingly important priority.

Nowadays, urban air pollution can be studied using a combination of ground-based measurement networks and satellite observations (Ialongo et al., 2020; Sannigrahi et al., 2021). Satellite observations have helped to investigate urban air pollution,
40 particularly in cities without a ground-based monitoring network (Beirle et al., 2019; Borsdorff et al., 2019). In past decades, improvements in the quality and spatial resolution of satellite measurements have allowed the detection of trends in air pollutants and the quantification of urban emissions (Lorente et al., 2019; Verstraeten et al., 2018; Wennberg et al., 2018). Several studies have focused on NO_x, using NO₂ observations from the SCanning Imaging Absorption spectroMeter for Atmospheric Cartography (SCIAMACHY), the Ozone Monitoring Instrument (OMI) and TROPOMI (Ding et al., 2017;
45 Lorente et al., 2019). At the resolution and sensitivity of TROPOMI, urban NO₂ enhancements can be detected readily, even in single satellite overpass. OMI derived NO₂ data have been used to quantify NO_x emissions, as well as the urban lifetime of NO₂, as demonstrated by Beirle et al. (2011) using the Exponentially Modified Gaussian function fit (EMG) method.

In the EMG method, the satellite observed exponential decay of NO₂ downwind of the city centre is used to quantify the first order loss of NO₂, driven primarily by its reaction with the hydroxyl radical (OH). Liu et al. (2016) modified the EMG method
50 for application to complex emission patterns. The quantification of CO emissions from cities is more complicated compared with NO₂ because of its longer lifetime, and the related importance of CO sources from the surroundings of cities. Nevertheless, a few studies have demonstrated the feasibility of quantifying relative changes in urban CO emission, using Measurement of Pollution in the Troposphere (MOPITT), Infrared Atmospheric Sounding Interferometer (IASI), Atmospheric Infrared Sounder (AIRS), and TROPOMI observations (Borsdorff et al., 2019; Dekker et al., 2017; Pommier et al., 2013).

55 In recent years, methods have been developed that combine satellite measurements of different trace gases, for example the combined use of NO₂ and CO, to obtain specific information about pollutant sources (Lama et al., 2020; Hakkarainen et al., 2015; Miyazaki et al., 2017; Reuter et al., 2019; S. Silva & Arellano, 2017). The emission factors of CO and NO_x from fuel combustion are uncertain and vary strongly with the combustion efficiency (Flagan and Seinfeld, 1988). The satellite observed NO₂/CO ratio is particularly sensitive to this fuel burning efficiency, as demonstrated by Lama et al., (2020) and can be used
60 to evaluate emission inventories. However, another important uncertainty arises from the removal of NO₂ by OH. OH is an important oxidant in the atmosphere, which determines the lifetime of trace gases such as CO, NO_x, sulphur dioxide (SO₂) and volatile organic compound (VOCs) (Monks et al., 2009). OH plays the important role in atmospheric chemistry on scales ranging from urban air pollution to the global residence times of greenhouse gases. The direct measurement of OH is possible

using spectroscopic methods, but the spatial representativeness of the data is limited due to its short lifetime (de Gouw et al., 2019). OH estimates from global Chemical Transport Models (CTM's), which has an uncertainty of > 50 % (Huijnen et al., 2019). Urban measurement campaigns point to large discrepancies between modelled and observed OH abundances, for example in Lu et al., (2013) who found a factor 2.6 difference in a campaign in the suburbs of Beijing.

The aim of this study is therefore to estimate the average OH concentration in the urban plume of large cities (hereafter referred to as urban OH) from the downwind decay of the TROPOMI observed NO₂/CO ratio. The proposed method makes use of the WRF model (Grell et al., 2005) to simulate the meteorological fields and atmospheric transport. The TROPOMI instrument (Veefkind et al., 2012), launched on 13 October 2017 on board the Sentinel-5 Precursor satellite, is particularly well suited for this task, as it measures both compounds with high sensitivity and spatial resolution. Our method uses CO, because it has a longer lifetime than NO₂ (weeks-months compared to a few hours). Therefore, CO can be considered as an inert tracer at the time-scale of urban plumes. The difference in the rate of decay between NO₂ and CO provides therefore information about the photochemical oxidation of NO₂, because atmospheric dispersion is expected to have a very similar impact on both tracers and therefore cancels out in their ratio. The use of the NO₂/CO ratio for estimating urban scale OH is further compared to the Exponentially Modified Gaussian function fit (EMG) method, using only satellite retrieved NO₂ (Beirle et al., 2011).

The city of Riyadh (24.63° N, 46.71°E) is chosen as a test case. Riyadh is an isolated city and a strong source of CO and NO₂ pollution (Beirle et al., 2019; Lama et al., 2020). The frequent clear sky conditions over Riyadh yield a large number of valid TROPOMI CO and NO₂ data. The signal to noise in TROPOMI is high enough to detect the enhancement of CO and NO₂ over Riyadh in a single overpass (Lama et al., 2020). Model results from the Copernicus Atmospheric Monitoring Service (CAMS) for Riyadh show a distinct seasonality in OH (see Fig S1), which we attempt to evaluate using TROPOMI data for summer and winter.

This paper is organized as follows: Section 2 describes the TROPOMI NO₂ and CO data, the WRF model setup that was used, and the optimization method that is used for estimating OH. Optimization results and comparisons between TROPOMI and WRF are presented in section 3, followed by a summary and conclusion of the main finding in section 4. Additional figures and information about the optimization method are provided in the Supplement.

2. Data and Method

2.1 TROPOMI NO₂ tropospheric column

We used the offline TROPOMI level 2 tropospheric column NO₂ [mole m⁻²] data from retrieval versions 1.2.x for 2018 and 1.3.x for 2019 available at <https://s5phub.copernicus.eu>; <http://www.tropomi.eu> (last access: 21 September, 2020). NO₂ data of versions 1.2.x and 1.3.x have minor processing differences such as removal of negative cloud fraction, better flagging and uncertainty estimation. However, they use the same retrieval algorithm applied to level-1b version 1.0.0 spectra (Babic et al., 2019) recorded by the TROPOMI UV-Vis module in the 405-465nm spectral range. The TROPOMI NO₂ DOAS software,

95 developed at KNMI, is used for the processing of NO₂ slant column densities (van Geffen et al., 2019). The improved NO₂ DOMINO algorithm of Boersma et al. (2018) has been used to translate slant columns into tropospheric column densities. In this algorithm, stratospheric contributions are subtracted from the slant column densities and the residual tropospheric slant column density is converted to tropospheric vertical column density using the air mass factor (AMF). The AMF depends on the surface albedo, terrain height, cloud height and cloud fraction (Eskes et al., 2018; Lorente et al., 2017). The comparison of
 100 MAX-DOAS ground based measurements in European cities shows that TROPOMI underestimates of NO₂ columns by 7 % to 29.7 % (Lambert et al., 2019). To avoid biases, we re-calculated the AMF by replacing the tropospheric AMF, which is based on a vertical NO₂ column simulated by TM5, with the WRF-chem equivalent (Boersma et al., 2016; Lamsal et al., 2010; Visser et al., 2019), using the equation provided in the Appendix A. During summer, the bias correction increases TROPOMI NO₂ by 5 to 10 % and in winter by 25% to 30 % in the urban plume over Riyadh, whereas background areas are less affected
 105 (see Fig S2).

2.2 TROPOMI CO

For CO, the offline level 2 CO data product version 1.2.2 has been used, available at <https://cophub.copernicus.eu/s5pexp> (last access: 20 September, 2020). The SICOR algorithm is applied to TROPOMI 2.3 µm spectra to retrieve CO total column density [molec cm⁻²] (Landgraf et al., 2016). The retrieval method is based on a profile scaling approach, in which TROPOMI-
 110 observed spectra are fitted by scaling a reference vertical profile of CO using the Tikhonov regularization technique (Borsdorff et al., 2014). The reference CO profile is obtained from the TM5 transport model (Krol et al., 2005). The averaging kernel (A) quantifies the sensitivity of the retrieved total CO column to variations in the true vertical profile (ρ_{true}), as follows (Borsdorff et al., 2018a):

$$C_{retrieval} = A \cdot \rho_{true} + \epsilon_{CO} \quad (1)$$

115 where, $C_{retrieval}$ is the retrieved column average CO mixing ratio, ϵ_{CO} is the retrieval error, statistically represented by the retrieval uncertainty that is provided for each CO retrieval.

2.3 Satellite Data Selection and Filtering Criteria

As NO₂ and CO are retrieved from different channels of TROPOMI using different retrieval algorithms, the filtering criteria and spatial resolutions of CO and NO₂ are different. The data filtering makes use of the quality assurance value (qa) and is
 120 provided with the CO and NO₂ retrievals, ranging from 0 (no data) to 1 (high quality data). We selected NO₂ retrievals with $qa \geq 0.75$ (clear sky condition) and CO retrievals with $qa \geq 0.7$ (clear sky or low level cloud) as in Lama et al., (2020). The SICOR algorithm was originally developed for SCIAMACHY to account for the presence of low elevation clouds, increasing the number of valid measurements (Borsdorff et al., 2018a). In addition, the CO stripe filtering technique is applied as described by Borsdorff et al. (2018). Using dry air column density derived from the surface pressure data in CO and NO₂ TROPOMI
 125 files, the total CO column and tropospheric NO₂ column densities are converted to dry column mixing ratios XCO (ppb) and

XNO₂ (ppb). The spatial resolution of the NO₂ data is finer compared to the CO data (3.5x7 km² versus 5.5x7 km²). After the CO and NO₂ retrievals pass the filtering criteria, their co-location is approximated by assigning the centre coordinates of an NO₂ retrieval to the CO footprint in which it is located (Lama et al., 2020).

2.4 Weather Research Forecast model (WRF)

130 We have used WRF- chemistry model (<http://www.wrf-model.org/>), version 3.9.1.1 to simulate NO₂ and CO mixing ratios over Riyadh. WRF is a non-hydrostatic model designed by the National Center for Environmental Protection (NCEP) for both atmospheric research and operational forecasting applications. For this study, we have setup three nested domains in the model at resolutions of 27 km, 9 km and 3 km, centred at 24.63°N, 46.71°E. The first and second domain cover Saudi Arabia and provide the boundary conditions for the nested third domain (see Fig. S3). The analysis in this paper uses the 500 x 500 km²
135 sub region around Riyadh in the third domain, containing 161 by 161 grid cells. All domains are extended vertically from the Earth's surface to 50 hPa, using 31 vertical layers, with 17 layers in the lowermost 1500 m. WRF simulations are performed using a time step of 90 seconds for the period June 2018 to March 2019, using a spin-up time of 10 days.

We have used the Unified Noah land surface model for surface physics (Ek et al., 2003; Tewari et al., 2004), an updated version of the Yonsei University (YSU) boundary layer scheme (Hu et al., 2013) for the boundary layer processes, and the
140 Rapid Radiative Transfer Method (RRTM) for short-wave and long-wave radiation (Mlawer et al., 1997). Cloud physics is solved with the new Tiedtke cumulus parameterization scheme (Zhang and Wang, 2017). The WRF Single Moment 6-class scheme is used for microphysics (Hong and Lim, 2006). The WRF coupling with chemistry (WRF-chem) allows the simulation of tracer transport and the chemical transformation of trace gases and aerosols. Here, we used the passive tracer transport function instead of the encoded chemistry in WRF to speed up the model simulation. In addition, the passive tracer
145 option helps in separating the influences of wind, OH and the rate constant of the NO₂+OH reaction ($K_{\text{NO}_2+\text{OH}}$) on the NO₂/CO ratio in the downwind city plume. The function of different tracers, their acronym and explanation of different WRF simulations is provided in Table 1.

The meteorological initial and boundary conditions are based on NCEP data at 1°x1° spatial and 6-hr temporal resolution available at <https://rda.ucar.edu/datasets/ds083.2/>. Nitrogen Oxides (NO_x = NO₂ +NO) and CO anthropogenic emissions
150 have been taken from the Emission Database for Global Atmospheric Research v4.3.2 (EDGAR) 2012 at 0.1°x0.1° spatial resolution (Crippa et al., 2016). The EDGAR 2012 data have been re-gridded to the resolution of the WRF domains and hourly, weekly and monthly emission variations are taken into account using the temporal emission factors provided by van der Gon et al. (2011). The chemical boundary conditions for CO and NO_x are based on the CAMS chemical reanalysis product at 0.75°x0.75° spatial, and 3-hourly temporal resolution (Inness et al., 2019), retrieved from
155 <https://ads.atmosphere.copernicus.eu/cdsapp#!dataset/cams-global-reanalysis-eac4?tab=form>, last access: 1st November, 2020). XCO and XNO₂ boundary condition based on CAMS is assumed to be representative as background value within the

domain. Since we do not explicitly compute the sources and sinks of background NO_2 inside the domain, we decide to transport the boundary conditions as background passive tracers.

Table 1. Summary of WRF simulations and the definition of tracers and acronym used.

WRF Simulation / Tracer	WRF input / Tracer definition
Prior	WRF run using NCEP meteorological data, EDGAR CO and NO_x emissions, CAMS OH, and CAMS CO and NO_x as initial and lateral boundary conditions.
WRF_{OH*1.1}	Prior run with CAMS OH increased by 10 %
Optimized run_{1st iter}	Optimized state (background, emission, OH) after iteration 1
Optimized run_{2nd iter}	Optimized state (background, emission, OH) after iteration 2
CO	
XCO_{emis}	The contribution of urban CO emissions to XCO
XCO_{Bg}	The contribution of the background to XCO
XCO_{WRF}	XCO from the Prior run
XCO_{WRF,1st iter}	XCO from Optimized run _{1st iter}
XCO_{WRF,opt}	XCO from Optimized run _{2nd iter}
NO₂	
XNO_{2 emis}	The contribution of urban NO_x emissions to XNO ₂ , ignoring the OH sink
XNO_{2 (emis,OH)}	As XNO _{2 (emis,OH)} accounting for the OH sink
XNO_{2 (emis,OH* 1.1)}	As XNO _{2(emis,OH)} with CAMS OH increased by 10 %
XNO_{2 Bg}	The contribution of the background to XNO ₂
XNO_{2 WRF}	XNO ₂ from the Prior run.
XNO_{2 (WRF ,OH* 1.1)}	XNO ₂ from WRF _{OH*1.1} .
XNO_{2 WRF 1st iter}	XNO ₂ from Optimized run _{1st iter}
XNO_{2 WRF opt}	XNO ₂ from Optimized run _{2nd iter}
Ratio (NO₂/CO)	
Ratio_{without OH}	Ratio of XNO _{2 emis} and XCO _{emis}
Ratio_{with OH}	Ratio of XNO _{2 (emis,OH)} and XCO _{emis}
Ratio_{Bg}	Ratio of XNO _{2 Bg} and XCO _{Bg}
WRF Ratio	Ratio of XNO _{2 WRF} and XCO _{WRF}
WRF Ratio_{OH*1.1}	Ratio of XNO _{2 (WRF,OH* 1.1)} and XCO _{WRF}
WRF Ratio_{1st iter}	Ratio of XNO _{2 WRF ,1st iter} and XCO _{WRF,1st iter}

160

The atmospheric transport in WRF causes the influence of NO_x and CO emissions from Riyadh on their column average mixing ratios to be linear. . In addition, we account for the chemical transformation of NO_x to HNO_3 in the reaction of NO_2 with OH. This is a simplified treatment of the lifetime of NO_x as other photochemical pathways play a role, such as:

165

- The oxidation of NO_2 in reaction with organic radicals (RO_2) to form the alkyl and multifunctional nitrates ($RONO_2$) (Romer Present et al., 2019)
- NO_x loss due to the formation dinitrogen pentoxide (N_2O_5) followed by heterogeneous transformation to HNO_3 (Shah et al., 2020).
- Peroxyacetyl nitrate (PAN) formation in equilibrium between NO_2 and the peroxyacetyl radical (Moxim, 1996).
- The dry deposition of NO_2 on the surface and plant stomata (Delaria et al., 2020).

170

The loss of NO_2 by OH to HNO_3 accounts for 60% of the global NO_x emission (Stavrakou et al., 2013). Macintyre and Evans.,(2010) showed that the N_2O_5 pathway reduces NO_x concentrations by 10 % in the tropics (30° N to 30° S) and 40 % at northern latitudes. The NO_x loss through N_2O_5 hydrolysis is largest at northern latitudes during winter (50 % to 150 %), unlike the tropics where its seasonality is small. Moreover, the removal of N_2O_5 is primarily important during night time because of its photolysis during daytime, whereas our analysis focuses on the midday overpass time (13:30) of TROPOMI

175

when OH abundances are highest. For these reasons, we consider it save to neglect the loss of NO_x through N_2O_5 in our analysis for Riyadh. The dry deposition flux is also expected to be low as it is controlled largely by stomatal uptake, which is assumed to be insignificant for the low vegetation cover of Riyadh. The same is expected to be true for PAN formation because of its thermal decomposition at increasing temperatures. We acknowledge that our OH estimates should be regarded as upper limits due to the neglect of other NO_x transformation pathways. A quantification of the combined effect would

180

require full chemistry simulations, which we consider outside of the scope of this paper.

Note that in this study, OH is only applied to the urban NO_x emission tracer ($XNO_{x(emis,OH)}$). The CAMS NO_x background tracer ($XNO_{x(Bg)}$) is transported in WRF without OH decay, since it already represents the balance between regional sources and sinks. CAMS hydroxyl radical (OH) data at a resolution of $0.75^\circ \times 0.75^\circ$ spatial and 3 hourly temporal resolution (Inness et al., 2019) retrieved at <https://ads.atmosphere.copernicus.eu/cdsapp#!/dataset/cams-global-reanalysis-eac4?tab=form>, last

185

access: 1st July, 2020) is spatially, temporally and vertically interpolated to the WRF grid. The NO_x lifetime is derived as follows:

$$\frac{dNO_2}{dt} = K_{NO_2 OH} \cdot [OH] \cdot [NO_2] \quad (2)$$

$$fact = \frac{NO_x}{NO_2} \quad (3)$$

$$\tau_{NOx} = \frac{1}{\frac{K_{NO_2 OH}}{fact} \cdot [OH]} \quad (4)$$

where, $K_{NO_2 OH}$ is the International Union of Pure and Applied Chemistry (IUPAC) 2nd order rate constant for the reaction of NO_2 with OH. “fact” represents the fractional contribution of NO_2 to NO_x (NO_x/NO_2). This NO_x to NO_2 conversion factor is derived from the CAMS reanalysis and re-gridded to WRF, to account for its spatial and temporal variation. τ_{NOx} is the lifetime of NO_x .

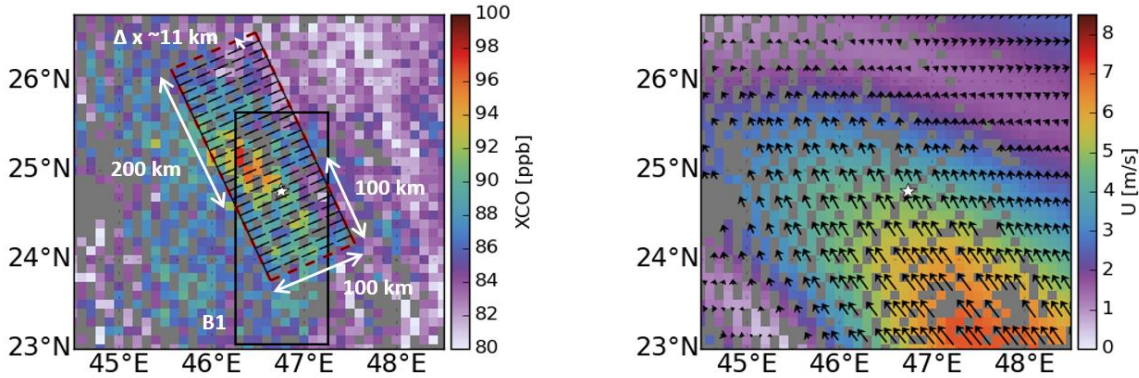


Figure 1. TROPOMI derived XCO (left) and average wind speed and wind direction from the surface to the top of boundary layer derived from the CAMS global reanalysis eac4 data at the TROPOMI overpass time over Riyadh for August 4th, 2018. The white star represents the centre of Riyadh. The black box (B1) with a dimension of 300 x 100 km² is rotated in the average wind direction at 50 km radius from the centre of Riyadh at the TROPOMI overpass time resulting in the red box. For the calculation of cross-directional averaged NO_2 and CO, the red box is divided into 29 smaller cells with the width (Δx) ~11 km. For this TROPOMI derived XCO is gridded at 0.1°x0.1°.

In earlier work with satellite NO_2 data, the Jet Propulsion Laboratory (JPL) high pressure limit was used as rate constant to represent the first order loss of NO_2 (Beirle et al., 2011; Lama et al., 2020; Lorente et al., 2019). However, we found this approximation to be too crude, and therefore apply the full IUPAC recommended pressure dependent formula for the 2nd order rate constant. Supplement Figure S4 shows the difference between the three rate constants, i.e. JPL high pressure limit, JPL 2nd order and IUPAC 2nd order, confirming the importance of accounting for the pressure dependence.

WRF output for the third domain is interpolated spatially and temporally to the footprints of TROPOMI. The interpolated WRF- NO_x tracers are converted to NO_2 using the conversion factor derived from the CAMS reanalysis accounting for its spatial and temporal variation (for the names and functions of tracers see Table 1). The averaging kernel available for each TROPOMI CO and NO_2 observation is applied to the WRF output, after interpolation to the vertical layers of the TROPOMI

retrieval. To compare WRF output to TROPOMI, WRF derived XNO_2 ($XNO_{2,WRF}$) is calculated by combining the NO_2 emission tracer that accounts for the OH effect ($XNO_{2,(emis,OH)}$) and the CAMS NO_2 background ($XNO_{2,Bg}$) (see Fig. S5 and S6). Similarly, the CO emission tracer (XCO_{emis}) is added to the CAMS CO background (XCO_{Bg}) to calculate WRF simulated XCO (XCO_{WRF}) (see Fig. S7 and S8).

2.5 NO_2/CO ratio calculation using box rotation

The variation of the NO_2/CO ratio in the downwind city plume is calculate as a function of distance x from the city centre in downwind direction. We select days with an average wind speed (U) in the range of 3.0 ms^{-1} (Beirle et al., 2011) $< U < 8.5\text{ ms}^{-1}$ (Valin et al., 2013) within a 50 km radius from the centre of Riyadh (24.63° N , 46.71° E). The horizontal distribution of EDGAR emissions over Riyadh is used within this 50 km radius (Fig S9). Ninety five days in summer and 70 days in winter meet the wind speed criteria over Riyadh for the ratio calculation. The boundary layer average wind speed and direction is calculated using the CAMS global reanalysis eac4 (retrieved at <https://ads.atmosphere.copernicus.eu/cdsapp#!/dataset/cams-global-reanalysis-eac4?tab=form>, last access : 1st August, 2020) at a resolution of $0.75^\circ \times 0.75^\circ$ spatial and 3 hourly temporal resolution. For this, the CAMS wind vector is spatially and temporally interpolated to the central coordinate of TROPOMI pixels.

To compute the NO_2/CO ratio as function of the downwind distance x , TROPOMI and WRF data have been re-gridded at $0.1^\circ \times 0.1^\circ$. A box (B1) is selected with a width of 100 km, from 100 km in upwind to 200 km in downwind direction of the city centre (see Fig 1a). The dimension of the box is motivated by multiple TROPOMI overpasses over Riyadh showing NO_2 and CO enhancements advected downwind over a ~ 200 km distance, without other large sources of NO_2 and CO within a 100 km radius of the city centre (see Fig. 1a). Figure 1(b) shows the boundary layer averaged wind speed and wind direction over Riyadh indicating flow towards the northeast on 4th of August, 2018. The box is rotated for every TROPOMI overpass depending upon the daily average wind direction within a 50 km radius from centre of Riyadh as shown in Figure 1(a) and Figure S10. The rotated box B1 is divided into N rectangular boxes, orthogonal to the wind direction with length (Δx) ~ 11 km (see Fig. 1 and Fig. S10). The XNO_2 and XCO grid cells that fall within the N rectangular boxes are selected to derive zonally averaged XNO_2 and XCO for summer and winter.

Unlike the enhancements over the city, ΔXNO_2 and ΔXCO become smaller than retrieval uncertainties at large distance from the city, where the ratio $\Delta XNO_2/\Delta XCO$ becomes ill-defined. Therefore, we decided to use the ratio of mean XNO_2 and XCO instead of enhancements over the background. To analyse the influence of atmospheric transport and the OH sink on the WRF derived XNO_2/XCO ratio two different ratios are derived: 1. $\frac{XNO_{2,emis}}{XCO_{emis}}$, named “Ratio_{without OH}”, 2. $\frac{XNO_{2,(emis,OH)}}{XCO_{emis}}$, named “Ratio_{with OH}” (see Table 1). The CAMS background accounts for the balance between regional source and sink in CTMs so it is excluded to analyse the influence of atmospheric transport on the ratio. For the comparison between TROPOMI and WRF, the CAMS backgrounds are included in “WRF RATIO” ($\frac{XNO_{2,WRF}}{XCO_{WRF}}$) (see Table 1). The comparison of WRF RATIO to TROPOMI ratio, and the contribution of its components, is presented in section 3.2.

240 2.6 OH estimation: satellite data only

In the EMG method, following Beirle et al. (2011), 2D NO₂ column densities maps are assigned to eight equal wind sectors, spanning 360 degree for summer and winter. 1D column densities per wind sector are computed by averaging in cross wind direction. This way, average NO₂ column density functions of the downwind distance to the city centre have been constructed for summer and winter (see Fig. S11). Using the EMG method as in Beirle et al., (2011), the e-folding distance x₀ and NO₂ emissions have been estimated. The NO₂ lifetime is derived by dividing x₀ by the average wind speed (5.46 ms⁻¹ and 5.24 ms⁻¹ for winter and summer, respectively) and is provided in Table 2. The OH concentration is derived from the inferred NO₂ lifetime using the IUPAC second order rate constant (for details see section S2 and S3). Using Eq. (4), the NO_x life time is derived. EMG derived NO₂ emissions are also converted to NO_x emissions using the CAMS-derived conversion factor. Summer and winter averaged CAMS derived conversion factors for the box of 300 km x 100 km are 1.28 and 1.31, respectively.

250 2.7 OH estimation: WRF optimization

To jointly estimate the NO_x and CO emissions as well as the OH concentration from the TROPOMI data, a least squares optimization method is used. This method fits the model to the data by minimizing a cost function (J) (see S1 for details). The reaction of NO₂ with OH introduces a non-linearity in the OH optimization. To account for this non-linearity, we linearize the problem around the a priori starting point, using small perturbations (10 %) Δ_{background}, Δ_{emission}, ΔOH. The non-linear model is fitted to the observations, by optimizing scaling factors f_{Bg}, f_{emis}, f_{OH} to the perturbation functions Δ_{background}, Δ_{emission} and ΔOH, respectively. This process is repeated iteratively, updating the linearization point and re-computing the perturbation functions.

We estimate OH by optimizing WRF with TROPOMI in two ways 1) optimizing the simulated NO₂/CO ratio using TROPOMI-derived ratios, named as “Ratio optimization” and 2) optimizing NO₂ and CO separately using TROPOMI derived XCO and XNO₂ named as “Component wise optimization”. First the ratio optimization is described followed by the component wise optimization. Optimized ratios are derived as follows:

$$F_{TROPOMI} = F + \frac{\Delta F}{\Delta_{emis}} * \frac{f_{emis}}{10} + \frac{\Delta F}{\Delta_{OH}} * \frac{f_{OH}}{10} + \frac{\Delta F}{\Delta_{Bg}} * \frac{f_{Bg}}{10} \quad (5)$$

$$F = \frac{XNO_{2\ WRF}}{XCO_{WRF}}$$

$$XNO_{2\ WRF} = XNO_{2\ (emis,OH)} + XNO_{2\ Bg} \quad (6)$$

$$265 \quad XCO_{WRF} = XCO_{emis} + XCO_{Bg} \quad (7)$$

$$\frac{\Delta F}{\Delta_{emis}} = \frac{XNO_{2\ (emis,OH)} * 1.05 + XNO_{2\ Bg}}{XCO_{emis} * 0.95 + XCO_{Bg}} - F \quad (8)$$

$$\frac{\Delta F}{\Delta OH} = \frac{XNO_2(emis,OH*1.1)+XNO_2Bg}{XCOemis+XCOBg} - F \quad (9)$$

$$\frac{\Delta F}{\Delta Bg} = \frac{XNO_2(emis,OH) + XNO_2Bg * 1.05}{XCOemis + XCOBg * 0.95} - F \quad (10)$$

Here, $F_{TROPOMI}$ is the TROPOMI derived NO_2/CO ratio, F is the WRF Ratio, $\frac{\Delta F}{\Delta emis}$ is the change in F due to an increase in the NO_2 emission by 5 % and a decrease in the CO emission by 5 % ($1.05/0.95 = \sim 10\%$), $\frac{\Delta F}{\Delta OH}$ is the change in F due to an increase in OH by 10 % and $\frac{\Delta F}{\Delta Bg}$ is the change in F due to an increase in the XNO_2 background by 5 % and a decrease in the CO background by 5 %. $XNO_2(emis,OH)$ is the contribution of city NO_x emissions to XNO_2 accounting for the OH sink, XNO_2Bg is the NO_2 background. $XCOemis$ is the contribution of the EDGAR city CO emissions to XCO and $XCOBg$ is the CO background derived from CAMS. XNO_{2WRF} and XCO_{WRF} is the WRF derived XNO_2 and XCO respectively.

$XNO_2(emis,OH*1.1)$ is the contribution of city NO_x emissions to XNO_2 after increasing CAMS OH by 10 %.

Although the ratio optimization is sensitive to the emission ratio and the OH sink of NO_2 , it is not sensitive to the absolute emissions of CO and NO_2 . Therefore, we performed component-wise optimizations for XCO and XNO_2 to optimize absolute emissions. We also compare the OH factor obtained from the ratio optimization and component-wise optimization to test the robustness of the method. The optimized XNO_2 is derived using Eq. (11). XCO is optimized using the same equation but without considering the OH sink (see Appendix B).

$$XNO_{2TROPOMI} = XNO_{2WRF} + \Delta XNO_{2emis} * \frac{f_{emis}}{10} + \Delta XNO_{2OH} * \frac{f_{OH}}{10} + \Delta XNO_{2Bg} * \frac{f_{Bg}}{10} \quad (11)$$

$$\Delta XNO_{2emis} = XNO_{2(emis,OH)} * 1.10 - XNO_{2(emis,OH)} \quad (12)$$

$$\Delta XNO_{2OH} = XNO_{2(emis,OH*1.1)} - XNO_{2(emis,OH)} \quad (13)$$

$$\Delta XNO_{2Bg} = XNO_{2Bg} * 1.10 - XNO_{2Bg} \quad (14)$$

Here, $XNO_{2TROPOMI}$ is the TROPOMI derived XNO_2 , XNO_{2WRF} is the WRF XNO_2 . ΔXNO_{2emis} is the change in XNO_2 due to an increase in emission by 10 %, ΔXNO_{2OH} is change in XNO_2 due to an increase in CAMS OH by 10 % and ΔXNO_{2Bg} is a change in the background XNO_2 by 10 %.

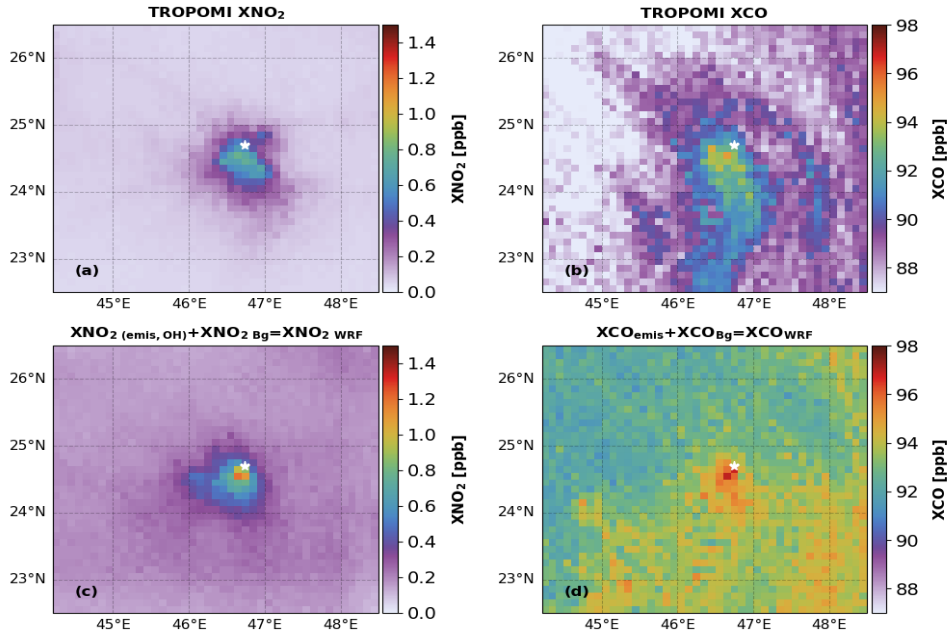


Figure 2. Comparison between XNO₂ (left) and XCO (right) from TROPOMI and WRF over Riyadh averaged over June to October, 2018. Top panels show TROPOMI data and bottom panels the corresponding co-located WRF results. **XNO₂_{WRF}** is derived by adding **XNO₂_(emis,OH)** and **XNO₂_{Bg}**. **XCO_{WRF}** is derived by adding **XCO_{emis}** and **XCO_{Bg}**. The white star represents the centre of city. TROPOMI and WRF results are gridded at 0.1°x0.1°.

3. Results and Discussion

290 3.1. XNO₂ and XCO over Riyadh

In this subsection, we compare WRF-derived XCO_{WRF} and XNO₂_{WRF} with TROPOMI for summer (see Fig. 2) and winter (see Fig. S6) over Riyadh. TROPOMI and WRF derived XCO and XNO₂ are averaged from June to October 2018 for summer and November 2018 to March 2019 for winter in a domain of 500 x 500 km² centered around Riyadh.

295 The comparison for summer in Figure 2 shows bias-corrected TROPOMI NO₂ after replacing the TM5-based tropospheric AMF with WRF profiles as described in Visser et al. (2019). The enhancement of XNO₂ and XCO over Riyadh due to urban emissions is clearly separated from the background for TROPOMI and WRF, showing that the city of Riyadh is well suited to investigate the use of the NO₂/CO ratio to quantify OH in urban plumes. Due to the longer life-time of CO, the TROPOMI-observed XCO plume extends further in the southeast direction compared to XNO₂. Figure 2 shows that our WRF simulations are able to reproduce the TROPOMI retrieved XNO₂ ($r^2 = 0.96$) and XCO ($r^2 = 0.78$) plumes, confirming that WRF-derived

300 $\frac{XNO_2_{WRF}}{XCO_{WRF}}$ is suitable for the optimization of CTM-derived OH concentrations using TROPOMI data. XNO_2_{WRF} is higher by 25 % compared to TROPOMI in the city centre. In the background, XCO_{WRF} shows a similar spatial distribution as TROPOMI XCO, but the values are higher by 5 to 10 % (see Fig 2.). Close to the city centre, XCO_{WRF} is ~5.7 % higher than TROPOMI XCO. In EDGAR 2011, emission sources are located in the centre of Riyadh (see Fig. S9). However, as noted by Beirle et al. (2019) they extend to a larger part of the city in reality. This difference in spatial distribution leads to higher XNO_2_{WRF} and
 305 XCO_{WRF} close to centre of Riyadh compared to TROPOMI.

In winter, the wind direction is predominantly from the south easterly sector in WRF and TROPOMI (see Fig S12). The spatial distribution of XCO_{WRF} ($r^2 = 0.73$) and XNO_2_{WRF} ($r^2 = 0.88$) matches quite well with TROPOMI. Therefore, the difference between summer and winter should offer the opportunity to quantify the seasonality in emissions and OH concentrations over Riyadh. In winter, XCO_{WRF} is ~5 to 10 % higher than TROPOMI, while XNO_2_{WRF} is higher by 40 % to 50 %. The difference
 310 could either point to uncertainties in the emission NO_2/CO emission ratio, uncertainties in the NO_2 lifetime, or inaccuracies in the background. By quantifying OH, we can evaluate these explanations (see section 3.3). XNO_2_{WRF} is higher by 20 % in winter than in summer. Contrary, TROPOMI NO_2 is lower by ~30 % in winter (Fig S12.) compared to summer (Fig. 2). Again, to disentangle the role of changing sources and sinks, we need an independent estimates of OH.

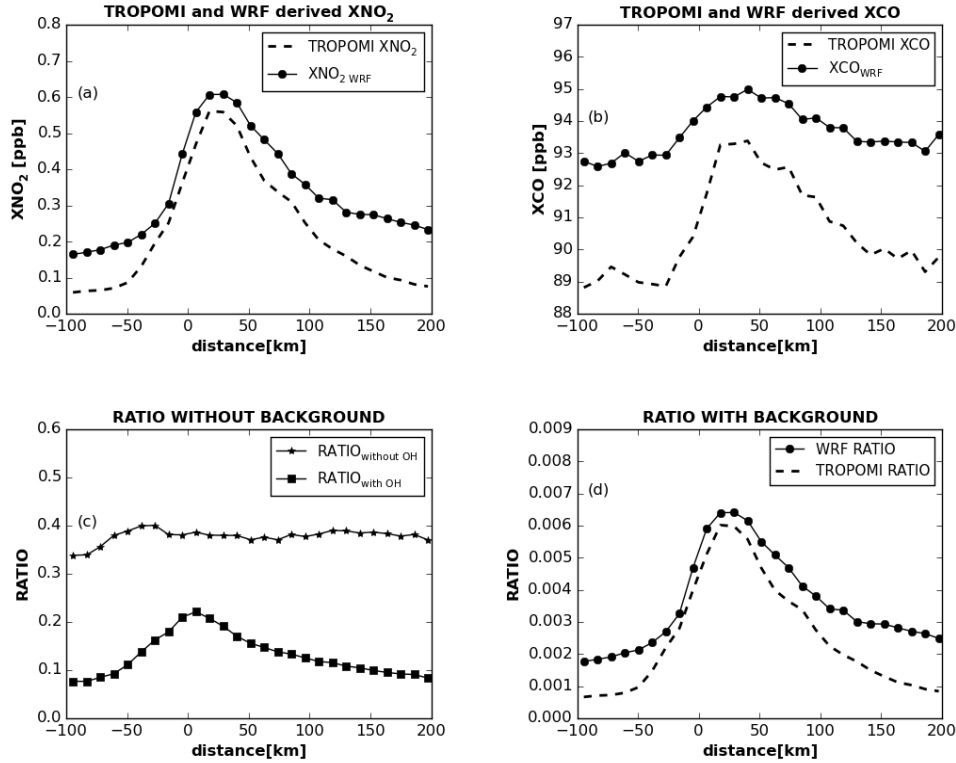


Figure 3. Comparison of WRF and TROPOMI zonally averaged a) XNO₂, b) XCO and c) WRF Ratio (XNO₂/ XCO) without CAMS background d) TROPOMI and WRF Ratio (XNO₂/ XCO) with background as a function of distance to the centre of Riyadh for summer (June, 2018 to October, 2019).

3.2. The XNO₂/XCO ratio and OH

Before comparing TROPOMI and WRF-derived XNO₂/XCO ratios, we first analyse the influence of atmospheric transport and the OH sink on the WRF derived XNO₂/XCO ratio. To do this three ratios are used 1. Ratio_{without OH} 2. Ratio_{with OH} 3. WRF RATIO (see Table 1). As seen in Figure 3, S13 and S14, WRF is able to reproduce the TROPOMI-observed downwind evolution of XNO₂ and XCO in summer and winter. The peak of the XNO₂ and XCO plumes is shifted away from the city centre due to the balance between the accumulation of urban emissions in the atmospheric column and atmospheric transport (Lorente et al., 2019).

As expected, Ratio_{without OH} shows an approximately straight line when the background is removed, because transport influences NO₂ and CO in the same way and therefore cancels out in the ratio (see Fig. 3b). The Ratio_{with OH} however, shows an approximately Gaussian relation with distance due to the influence of the sink on NO₂. This comparison demonstrates the

325 sensitivity of the relation between XNO_2/XCO ratio and downwind distance to the NO_2 lifetime, which we want to exploit to quantify OH. When including the background, the shapes of the functions in Figure 3c change (not shown), because the relative weights of the background and city contributions to the ratio vary with distance of the city centre. In summer, the WRF RATIO is higher by ~15 % close to centre of city TROPOMI due to the overestimation of $XNO_{2\text{ WRF}}$ in WRF (see Fig. 3d). However in the downwind plume, at a distance of 100 km WRF RATIO is higher by 20 to 50 % compared to TROPOMI.

330 In winter, $Ratio_{\text{without OH}}$ and $Ratio_{\text{with OH}}$ show relations with downwind distance that are similar to summer, confirming that an OH sink leads to a Gaussian structure of the ratio (see Fig. S14). The winter WRF RATIO is 49 % higher than TROPOMI due to the overestimation of XNO_2 by 40 to 50 %. The WRF RATIO close to the centre of city is also 20% higher in winter than in summer, due to higher winter $XNO_{2\text{ WRF}}$ than in summer (see Fig S12 and S15). In contrast, TROPOMI shows a higher ratio in summer compared to winter (see Fig S15). These differences between TROPOMI and WRF-derived

335 ratios offer an opportunity to address uncertainties in CTM computed urban OH and emission inventories, which will be explored next.

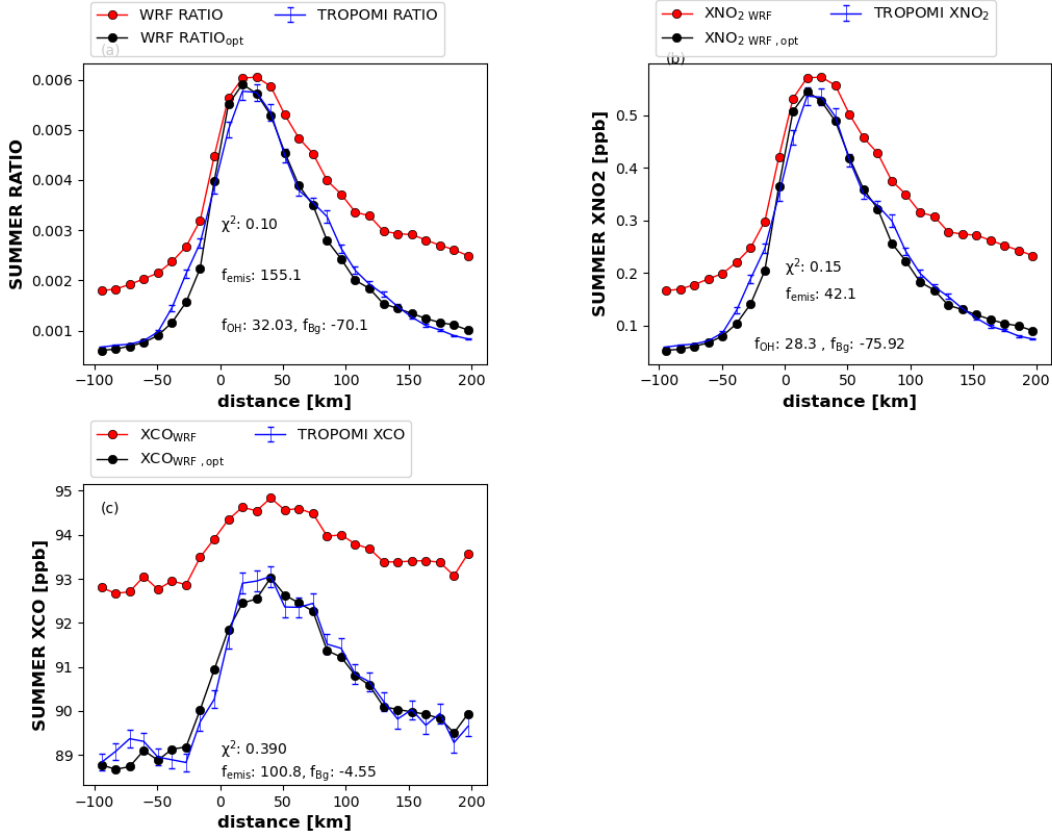


Figure 4. Comparison between TROPOMI and WRF, before and after optimization for Summer (averaged over June to October, 2018). a) XNO₂/XCO ratio, b) XNO₂ and c) XCO in comparison to TROPOMI. f_{OH} , f_{emis} and f_{Bg} are optimized scaling factors obtained iteratively for OH, emissions and background by least square optimization method. f_{emis} , f_{OH} and f_{Bg} are derived by accounting the total change in emission, OH and background using the corresponding scaling factors obtained from 1st and 2nd iterative step. The unit of scaling factor is in percent (%).

3.3 WRF optimization

To translate the discrepancies between TROPOMI and WRF derived ratios of section 3.2 into implied differences in emissions and OH, the least squares optimization method has been used as described in section 2.6. Before optimizing WRF using TROPOMI, pseudo data experiments in WRF have been carried out to test if the optimization method is capable of recovering true emissions and OH levels. To this end, changes in OH concentrations, emissions and background by known scaling factors have been applied to the WRF prior simulation to create a synthetic dataset. This process is repeated multiple times to create thousands of synthetic datasets. Subsequently, the scaling factors are obtained in the inversion procedure. These tests reveal that the estimation errors for f_{emis} , f_{OH} and f_{Bg} are less than 2.5 % (see Fig. S16). This confirms that the least square optimization method works, with two iterations leading to a sufficient accuracy, and can be used to estimate emissions and OH from TROPOMI data. Using TROPOMI data, estimation errors for f_{emis} , f_{OH} and f_{Bg} are expected to be higher due to atmospheric transport errors, simplified chemistry, and XCO and XNO₂ retrieval uncertainties. These errors did not play a role in the pseudo-data experiments, in which perfect transport and sampling was assumed. The results for summer are summarized in

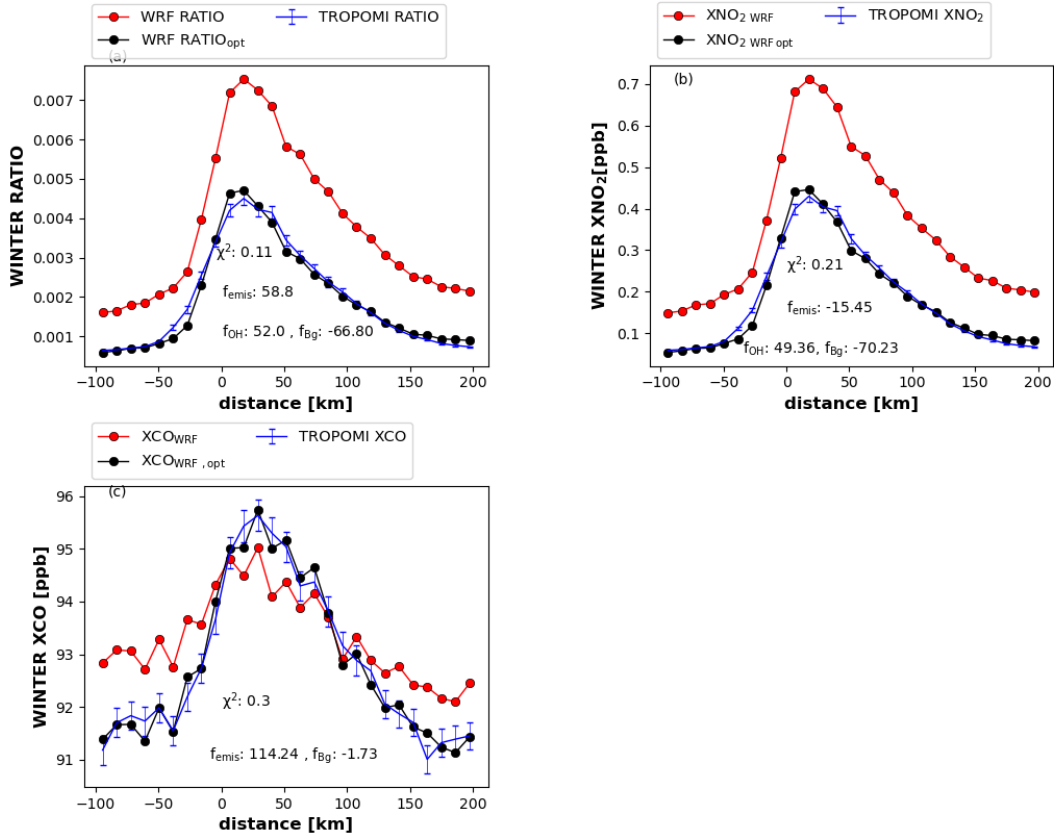


Figure 5. As Figure 4, for Winter (averaged over November, 2018 to March, 2019)

350 Figure 4, showing the optimized fit to the TROPOMI data as well as the corresponding scaling factors f_{emis} , f_{OH} and f_{Bg} that are estimated. The optimized emission, OH and Bg obtained from 2nd iteration is divided by Prior to derive the f_{emis} , f_{OH} and f_{Bg} . The results of iterative step for summer and winter is shown in Fig S17 and S18.

Figure 4a shows WRF ratios for summer in comparison to TROPOMI, before and after optimizing the OH concentration. The optimized WRF ratios fit the TROPOMI ratios well with $X^2 = 0.1$ (for the derivation of X^2 see section S4). The estimated
355 uncertainties for the scaling factors f_{emis} , f_{OH} and f_B are derived by summing the contribution of wind speed, length and width of box and NO₂ bias correction in quadrature as provided in Tables S1 and S2. For summer and winter, the uncertainties of the optimized OH concentrations range from 11 % to 15 %. For NO_x and CO emissions, these uncertainty ranges are ~25 % and ~10 to 15 %, respectively. According to the ratio optimization, the CAMS OH and the emission ratio are underestimated by 32.03 ± 4.0 % and 155.1 ± 14.9 % respectively. The CAMS background ratio is overestimated by 70.1 ± 6.2 %. It should be
360 realized here that the ratio optimization does not estimate the absolute emission of NO₂ and CO, but only their ratio.

To investigate the implication of this, we performed component-wise optimizations of WRF-derived XCO_{WRF} and $XNO_{2\ WRF}$. Optimized XCO_{WRF} and $XNO_{2\ WRF}$ fit well to the TROPOMI data (see Fig. 4b and 4c). In the XNO_2 optimization, the EDGAR NO_x emission is increased by 42.1 ± 9.5 % and the CAMs background is reduced by 75.92 ± 10.0 %. OH is increased by 28.3 ± 3.7 %, close to the results obtained from the ratio optimization. In the XCO optimization, EDGAR CO emissions are roughly
365 doubled and the background is reduced by 4.55 ± 0.5 % compared to CAMS. The ratio optimization suggests to increase the prior emission ratio 0.68 by 155.1%. The summer optimized NO_x/CO emission ratio derived from the component wise optimization is 0.38. The optimized emission ratio from ratio optimization is larger by factor 4.7 compared to component wise optimization. The difference between two estimates can be explained by different constraints on the solution in the two methods. In particular, the ratio inversion allows emission adjustment in a fixed relation between NO₂ and CO emissions
370 whereas the component wise has the full flexibility to adjust CO and NO₂ emission. The difference between the two estimates is larger than expected but does not affect the OH estimation. Lama et al., (2020) calculated TROPOMI derived summer emission (NO₂/CO) ratio for 2018 over Riyadh and mentioned that Monitoring Atmospheric Chemistry and Climate and CityZen (MACCity) emission ratio is more consistent with the TROPOMI derived ratio than EDGAR. The optimized emission ratio obtained from component wise optimization is consistent to Lama et al., (2020) and MACCity summer emissions. This
375 shows that for the accurate estimation of the emission and emission ratio, the component wise optimization method is preferable.

Figure 5 presents optimization results for winter, where optimized WRF is in similar good agreement with TROPOMI as for summer with $X^2 = 0.11$. For winter, the ratio optimization increases OH by 52.0 ± 5.3 % and the emission ratio by 58.8 ± 30.2 %. The ratio and component-wise optimizations again show similar OH adjustments, demonstrating the robustness of our
380 method. The background ratio is reduced by 66.80 ± 5.8 %. The component-wise optimization for XNO_2 reduces the EDGAR NO_x emission by 15.45 ± 3.4 % and the CAMS background by 70.23 ± 6.1 %. For XCO , the WRF XCO_{Bg} is reduced by 1.73 ± 0.1

% in combination with a doubling of the EDGAR CO emission. The optimized emission ratio (NO_x/CO) derived from component wise optimization is 0.33 which is lower by 3.5 times than optimized emission ratio obtained from ratio optimization.

Table 2. Overview of WRF optimized OH and NO_x emissions for Riyadh and comparison to the EMG method. The estimated uncertainty for EMG and WRF derived NO_x emission and OH concentration is the sum of the contribution of wind speed, length and width of box and NO₂ bias correction provided in Table S1, S2 and S3.

Parameter	Summer		Summer EMG	Winter		Winter EMG
	WRF Optimization			WRF Optimization		
	Prior	After		Prior	After	
NO _x emission (kg/second)	8.2	11.6±2.4	8.6±1.2	9.4	7.9±1.8	5.3±1.5
OH (1e ⁷ , molecules/cm ³)	1.3	1.7 ± 0.2	1.4 ± 0.2	0.86	1.3 ±0.14	1.2 ± 0.1
NO _x lifetime (hr)	3.1	2.4 ± 0.4	2.9 ± 0.3	4.9	3.3 ± 0.3	3.6 ± 0.3

To investigate the consistency between our method and the EMG method, the derived NO_x lifetimes, emissions and OH concentrations using both methods are listed in Table 2 for winter and summer. Our optimization and the EMG method agree well on the seasonal change in NO_x emission and OH concentration. Both methods result in higher NO_x emissions and shorter lifetimes in summer; lower NO_x emissions and longer lifetimes in winter. Riyadh has a dry and warm summer days and the increase in power consumption due to the use of air conditioning contributes to the higher emission in summer than in winter (Lange et al., 2021). During the summer, EMG and the WRF optimization method both increase the NO_x emission and OH concentration compared with the prior. The size of the NO_x emission and OH concentration increase, obtained using the WRF optimization method is higher than the EMG method by 15% to 29 %. However, the difference between the EMG method and the component optimization method are smaller compare to the uncertainty of the emission and OH concentration derived for the optimization method. For winter, the dissimilarity between the EMG method and the prior reduces after optimization. The NO_x emission after optimization differs from the EMG method by 33 %. Optimized OH concentration and NO_x lifetime differs by <10 % compared to EMG method. In general, the difference between the EMG and optimization results is within the uncertainty range of 20 to 30 %, confirming their consistency and strengthening the confidence in the estimates that are obtained from TROPOMI data.

In contrast to EMG method, the optimization method can be used for a single TROPOMI overpass and does not require yearly averaged NO₂ data. Segregation and averaging of NO₂ urban plume by wind sector is not required in the optimization method. The effect of transport cancels out in taking the NO₂ /CO ratio and loss of NO₂ is mostly governed by OH during the mid-day. In this study, NO_x emission and OH concentration is estimated iteratively whereas the EMG method arrives at the solution in a single step. However, since our optimization method requires a WRF model simulation it is computationally more expensive. Uncertainties in transport may create mismatches with the satellite observations, leading to errors in the optimized fit. This influences the quality of derived emission estimates (Dekker et al., 2017). Therefore, finding a simplified approach using satellite data to derive the emission ratio and to estimate OH concentration in urban plumes will be our focus in the future.

It should be realized that the a priori EDGAR emissions and TROPOMI optimized estimates represent different years (2012 and 2018, respectively). To check whether the emission differences that are found may be explained by trends in emissions, we compare EDGAR 2012 NO_x and CO emissions with 2018 accounting for seasonal and diurnal emission variations using temporal emission factors by van der Gon et al., (2011). EDGAR 2018 NO_x and CO emissions are derived by linear extrapolation using emission from 2000 to 2015 (see Figure S19). For summer mid-day NO_x emissions, the EDGAR emissions increased by 17.7 % from 2012 to 2018, which is lower than our optimization results. For winter, mid-day NO_x emissions increase in EDGAR by 13 % from 2012 to 2018, whereas the WRF optimization yield reductions by 15.6%. In EDGAR, summer and winter CO emissions increased from 2012 to 2018 by 25.5 % and 20.0 %, respectively. However, the WRF optimization suggests that the EDGAR CO emissions for summer and winter need to be doubled (see Table S4). Borsdorff et al., (2018b) mentioned that EDGAR CO emissions has to be increased significantly to match with TROPOMI CO observations over middle eastern cities such as Tehran, Yerevan, Tabriz and Urmia. Overall , this points to a significant uncertainty in the EDGAR emission inventory at the city scale.

To test the accuracy of the linear extrapolation of EDGAR data, we compare the relative change in NO_x and CO emission in 2012 to 2018 using CAMS Global (CAMS–GLOB) anthropogenic v4.2 emission datasets (<https://ads.atmosphere.copernicus.eu/cdsapp#!/dataset/cams-global-emission-inventories?tab=overview>). CAMS –GLOB shows that for summer and winter NO_x emission increases by 26 % from 2012 to 2018, which is higher by a factor 2 than EDGAR. CAMS-GLOB based summer and winter CO emission increases by 20 % from 2012 to 2018 which differs by ~20 % compared to EDGAR. In general, the relative increase in CO and NO_x emission from EDGAR and CAMS-GLOB is much smaller compared to the difference with our optimization method.

We realise that our method only considers the first order loss of NO₂ by OH forming HNO₃. In reality, the NO₂ lifetime is influenced by more spatially and temporally varying factors such as temperature, ozone, and radiation (Lang et al., 2015; Romer et al., 2018). In cities, the loss of NO₂ via the formation of alkyl and multifunctional nitrates (RONO₂) are also important reactions influencing the lifetime of NO₂ (Browne et al., 2013; Sobanski et al., 2017). For CO, secondary production from

short-lived volatile organic compounds can also play an important role in urban pollution plumes. The application of full chemistry that includes all the sources and losses of NO_2 and CO could therefore further improve the accuracy of OH estimates.

Another complicating factor is the strong variation in chemical regime that is expected in city air pollution plumes. Close to high NO_x sources, OH tends to be titrated away by the NO_2 (Valin et al., 2011). Further from the source, chemical conditions may be favorable for OH formation and recycling, reducing the NO_2 lifetime. To investigate this in order to refine the OH estimates presented in this paper, again a full chemistry framework would be required.

Figure S20 shows that power plants and manufacturing industries are the largest pollutant emitter over Riyadh (Beirle et al., 2019). In this study, NO_x and CO anthropogenic emissions are introduced at the surface, whereas the emission height of different sources is expected to vary in reality. The different emission heights for NO_x and CO emission sources can also influence the result. In the future, realistic emission heights should also be incorporated in WRF for accurate estimation of OH. Moreover, the temporal emission factors that have been used by van der Gon et al., (2011) are based on European countries. The comparison of van der Gon et al., (2011) with the Copernicus Atmosphere Monitoring Service TEMPORal profiles (CAMS-TEMPO) suggests that temporal emission factors for weekend road transport and monthly residential combustion are different in Riyadh compared to European countries. Road transport, CO emission has the largest contribution ~75 % to the total emission over Riyadh, whereas NO_x emission from road contributes by 24 % to the total NO_x emission. Residential combustion has the smallest contribution of ~0.3 to 0.4 % to total NO_x and CO emissions (see Fig S20). In the future, the application of accurate diurnal emission factors for road transport can further improve the accuracy of urban OH concentrations estimated using TROPOMI derived XNO_2/CO ratios. In addition, the seasonality for NO_x and CO emissions is different in Riyadh than in Europe, which should be accounted for in future studies also.

5 Conclusions

In this study, a new method is presented for estimating OH concentrations in urban plumes using TROPOMI observed XNO_2/XCO ratios in combination with WRF simulations of the downwind pollution plume of large cities. Our new method has been tested for the city of Riyadh using synthetic as well as real TROPOMI data. Seasonal emissions and OH concentrations have been estimated for summer (June to October, 2018) and winter (Nov, 2018 to March, 2019).

WRF is well able to reproduce the spatial distribution of TROPOMI retrieved XNO_2 and XCO plumes over Riyadh during the summer and winter seasons. However, the TROPOMI observed level of XNO_2 is lower than simulated using WRF by 25 % in summer and 40 to 50 % in winter. In both seasons, TROPOMI XCO agrees within 10 % with WRF. The variation in XNO_2 , XCO and their ratio as a function of downwind distance to the centre of Riyadh agrees well between WRF and TROPOMI. However, the WRF derived XNO_2/XCO ratio is higher by 15 % to 30 % in summer and 49 % in winter compared to TROPOMI, explained mostly by the difference in XNO_2 .

The differences between WRF and TROPOMI observations have been used to optimize emissions and the NO₂ lifetime. To this end, scaling factors for the city emissions, OH and the background level have been optimized iteratively using a least squares method. Ratio and component wise optimizations have been compared to test the overall consistency of the method. In summer, the ratio and XNO₂ optimization for XNO₂ suggest that the OH prior from CAMS is underestimated by 32.03±4.0
470 %. Estimates obtained from the ratio and NO₂-only optimization agree within 10 %, demonstrating the robustness of the method. Summertime emissions of NO_x and CO from EDGAR are increased by 42.1±8.7 % and 100.8±9.5 %. For winter, the ratio and component wise optimizations increase OH by ~52.0±5.3 % to fit TROPOMI inferred ratios. In the optimization of winter data, NO_x emissions are reduced by 15.45± 3.4 % and CO emissions are doubled. In the future, the remaining differences between TROPOMI observations and WRF simulations could be reduced further by the use of precise temporal
475 and monthly emission factors, emission heights and full chemistry to account for secondary sources of CO and NO₂.

TROPOMI inferred OH concentrations obtained from the least squares optimization method have been compared to the EMG method. For the summer, the optimized OH concentrations differ by 18 %, whereas they are within 7.5 % during winter. These results confirm that urban emissions and OH concentrations can robustly be estimated from TROPOMI data. With our method, single TROPOMI overpass can be used to estimate OH whereas EMG method requires averaging of NO₂ urban plume by wind
480 sector. The iterative approach allows to test the factors i.e. f_{emis} , f_{oh} and f_{bg} obtained from optimization method, whereas EMG method does not allows such flexibility.

An important remaining uncertainty is the bias correction of the TROPOMI XNO₂ retrieval. Following the recommended procedure, the air mass factor AMF is recalculated by replacing the tropospheric AMF based on TM5, that is provided with the data, with WRF-chem. The TROPOMI XNO₂ bias correction increases the mixing ratio in the urban plume of Riyadh by
485 5 to 10 % in summer and 25 to 30 % in winter. The background is less affected by the bias correction. Without TROPOMI XNO₂ bias correction, the uncertainty in scaling factor for OH can vary up to 20 % and NO_x emission to 60 % over Riyadh.

Appendix A: AMF recalculation

The air mass factor (AMF) used in the retrieval of TROPOMI XNO₂ has been re-calculated by replacing the tropospheric AMF, calculated from the NO₂ column simulated by TM5, with its WRF-chem equivalent, as described by Lamsal et al. (2010)
490 and Boersma et al. (2016) using the following Eq. (16),

$$M_{trop, WRF} = M_{trop, TM5} \times \frac{\sum_{l=1}^L A_{trop,l} x_{l,WRF}}{\sum_{l=1}^L x_{l,WRF}} \quad (16)$$

where, $M_{trop,WRF}$ and $M_{trop,TM5}$ are the tropospheric air mass factors derived from WRF and TM5, respectively. $A_{trop,l}$ is the tropospheric averaging kernel, ranging from the surface to the uppermost layer of the troposphere in the TM5 model (l). $x_{l,WRF}$ is the equivalent NO₂ column density in model layer l, based on WRF. A_{trop} in Eq. (16) is derived using $A_{trop} = A \times$

495 $\frac{M}{M_{trop}}$, where M and M_{trop} are the total and tropospheric AMF's respectively. Finally, the bias corrected NO_2 vertical column density is computed using,

$$NO_{2, \text{ bias corrected}} = \frac{M_{trop, TM5}}{M_{trop, WRF}} \times NO_2$$

where, NO_2 is the TROPOMI tropospheric NO_2 vertical column density and $NO_{2, \text{ bias corrected}}$ is the bias corrected TROPOMI tropospheric NO_2 vertical column density.

500 **Appendix B**

The component wise optimization of XCO_{WRF} to estimate the emission and background of CO uses the following equation,

$$XCO_{TROPOMI} = XCO_{WRF} + \Delta XCO_{emis} * \frac{f_{emis}}{10} + \Delta XCO_{Bg} * \frac{f_{Bg}}{10}$$

$$XCO_{WRF} = XCO_{emis} + XCO_{Bg}$$

$$\Delta XCO_{emis} = XCO_{emis} * 1.10 - XCO_{emis}$$

$$505 \quad \Delta XCO_{Bg} = XCO_{Bg} * 1.10 - XCO_{Bg}$$

Here, $XCO_{TROPOMI}$ is TROPOMI XCO, XCO_{WRF} is the WRF simulated XCO accounting for emissions and background CO, XCO_{emis} is the XCO contribution from the urban CO emission and XCO_{Bg} is the CAMS-derived XCO background. ΔXCO_{emis} is the change in XCO due to emission and ΔXCO_{Bg} is the change in the XCO background level.

Data Availability Statement. TROPOMI CO and NO_2 data can be downloaded from <https://cophub.copernicus.eu/s5pexp>.
510 EDGAR emission data is available at https://edgar.jrc.ec.europa.eu/emissions_data_and_maps. CAMS data can be downloaded from <https://ads.atmosphere.copernicus.eu/cdsapp#!/dataset/cams-global-reanalysis-eac4?tab=form>. WRF simulations output are available at <https://zenodo.org/deposit?page=1&size=20>

Author contributions. SL performed the data analysis, data interpretation, and wrote the paper. SH supervised the study. SH,
515 FKB, IA, MK and HACDG discussed the results. All co-authors commented on the paper and improved it.

Competing interests. The authors declare that they have no conflict of interest.

Acknowledgments.

We are thankful to the team that designed the TROPOMI instrument, consisting of the partnership between Airbus Defence
520 and Space Netherlands, KNMI, SRON, and TNO, commissioned by NSO and ESA. This work is supported by NWO GO
programme (grant no. 2017.036). We acknowledge the free availability of WRF-Chem model (<http://www.wrf-model.org/>).
Thanks to SURFSara for making the Cartesius HPC platform available for computations via computing grant no. 17235.

References

- Babic, L., Braak, R., Dierssen, R., Kissi-Ameyaw, J., Kleipool, J., Leloux, J., Loots, E., Ludewig, A., Rozemeijer, N.,
525 Smeets, S., and Vacanti, G.: Algorithm theoretical basis document for the TROPOMI L01b data processor Erwin Loots
Quintus Kleipool, : S5P-KNMI-L01B-0009-SD , issue 9.0.0, available at :
<https://sentinel.esa.int/documents/247904/2476257/Sentinel-5P-TROPOMI-Level-1B-ATBD>, (last access: 3rd Jan, 2020),
2019.
- Beirle, S., Boersma, K. F., Platt, U., Lawrence, M. G. and Wagner, T.: Megacity emissions and lifetimes of nitrogen oxides
530 probed from space, *Science* (80-.), 333(6050), 1737–1739, doi:10.1126/science.1207824, 2011.
- Beirle, S., Borger, C., Dörner, S., Li, A., Hu, Z., Liu, F., Wang, Y. and Wagner, T.: Pinpointing nitrogen oxide emissions from
space, *Sci. Adv.*, 5(11), 1–7, doi:10.1126/sciadv.aax9800, 2019.
- Boersma, K. F., Vinken, G. C. M. and Eskes, H. J.: Representativeness errors in comparing chemistry transport and chemistry
climate models with satellite UV-Vis tropospheric column retrievals, *Geosci. Model Dev.*, 9(2), 875–898, doi:10.5194/gmd-
535 9-875-2016, 2016.
- Boersma, K. F., Eskes, H. J., Richter, A., De Smedt, I., Lorente, A., Beirle, S., Van Geffen, J. H. G. M., Zara, M., Peters, E.,
Van Roozendaal, M., Wagner, T., Maasakkers, J. D., Van Der A, R. J., Nightingale, J., De Rudder, A., Irie, H., Pinardi, G.,
Lambert, J. C. and Compernelle, S. C.: Improving algorithms and uncertainty estimates for satellite NO₂ retrievals: Results
from the quality assurance for the essential climate variables (QA4ECV) project, *Atmos. Meas. Tech.*, 11(12), 6651–6678,
540 doi:10.5194/amt-11-6651-2018, 2018.
- Borsdorff, T., Hasekamp, O. P., Wassmann, A. and Landgraf, J.: Insights into Tikhonov regularization: Application to trace
gas column retrieval and the efficient calculation of total column averaging kernels, *Atmos. Meas. Tech.*, 7(2), 523–535,
doi:10.5194/amt-7-523-2014, 2014.
- Borsdorff, T., Andrased, J., De Brugh, J. A., Hu, H., Aben, I. and Landgraf, J.: Detection of carbon monoxide pollution from
545 cities and wildfires on regional and urban scales: the benefit of CO column retrievals from SCIAMACHY 2.3 μm
measurements under cloudy conditions, *Atmos. Meas. Tech.*, 11(5), 2553–2565, doi:10.5194/amt-11-2553-2018, 2018a.

- Borsdorff, T., Aan De Brugh, J., Hu, H., Hasekamp, O., Sussmann, R., Rettinger, M., Hase, F., Gross, J., Schneider, M., Garcia, O., Stremme, W., Grutter, M., Feist, Di. G., Arnold, S. G., De Mazière, M., Kumar Sha, M., Pollard, D. F., Kiel, M., Roehl, C., Wennberg, P. O., Toon, G. C. and Landgraf, J.: Mapping carbon monoxide pollution from space down to city scales with daily global coverage, *Atmos. Meas. Tech.*, 11(10), 5507–5518, doi:10.5194/amt-11-5507-2018, 2018b.
- Borsdorff, T., Aan de Brugh, J., Hu, H., Aben, I., Hasekamp, O. and Landgraf, J.: Measuring Carbon Monoxide With TROPOMI: First Results and a Comparison With ECMWF-IFS Analysis Data, *Geophys. Res. Lett.*, 45(6), 2826–2832, doi:10.1002/2018GL077045, 2018c.
- Borsdorff, T., Aan De Brugh, J., Pandey, S., Hasekamp, O., Aben, I., Houweling, S. and Landgraf, J.: Carbon monoxide air pollution on sub-city scales and along arterial roads detected by the Tropospheric Monitoring Instrument, *Atmos. Chem. Phys.*, 19(6), 3579–3588, doi:10.5194/acp-19-3579-2019, 2019.
- Browne, E. C., Min, K. E., Wooldridge, P. J., Apel, E., Blake, D. R., Brune, W. H., Cantrell, C. A., Cubison, M. J., Diskin, G. S., Jimenez, J. L., Weinheimer, A. J., Wennberg, P. O., Wisthaler, A. and Cohen, R. C.: Observations of total RONO₂ over the boreal forest: NO_x sinks and HNO₃ sources, *Atmos. Chem. Phys.*, doi:10.5194/acp-13-4543-2013, 2013.
- Crippa, M., Janssens-Maenhout, G., Dentener, F., Guizzardi, D., Sindelarova, K., Muntean, M., Van Dingenen, R. and Granier, C.: Forty years of improvements in European air quality: Regional policy-industry interactions with global impacts, *Atmos. Chem. Phys.*, doi:10.5194/acp-16-3825-2016, 2016.
- Dekker, I. N., Houweling, S., Aben, I., Röckmann, T., Krol, M., Martínez-Alonso, S., Deeter, M. N. and Worden, H. M.: Quantification of CO emissions from the city of madrid using MOPITT satellite retrievals and WRF simulations, *Atmos. Chem. Phys.*, 17(23), 14675–14694, doi:10.5194/acp-17-14675-2017, 2017.
- Delaria, E. R., Place, B. K., Liu, A. X. and Cohen, R. C.: Laboratory measurements of stomatal NO₂ deposition to native California trees and the role of forests in the NO_x cycle, *Atmos. Chem. Phys.*, 20(22), 14023–14041, doi:10.5194/acp-20-14023-2020, 2020.
- Ding, J., Miyazaki, K., Van Der A, R. R., Mijling, B., Kurokawa, J. I., Cho, S. Y., Janssens-Maenhout, G., Zhang, Q., Liu, F. and Felicitas Levelt, P.: Intercomparison of NO_x emission inventories over East Asia, *Atmos. Chem. Phys.*, 17(16), 10125–10141, doi:10.5194/acp-17-10125-2017, 2017.
- Ek, M. B., Mitchell, K. E., Lin, Y., Rogers, E., Grunmann, P., Koren, V., Gayno, G. and Tarpley, J. D.: Implementation of Noah land surface model advances in the National Centers for Environmental Prediction operational mesoscale Eta model, *J. Geophys. Res. Atmos.*, 108(22), 1–16, doi:10.1029/2002jd003296, 2003.
- Eskes, H.J., van Geffen, J., Boersma, K.F., Eichmann, K.-U, Apituley, A., Pedernana, M., Sneep, M., Pepijn, J., Loyola, D.: Level 2 Product User Manual Henk Eskes, S5P-KNMI-L2-0021-MA, issue 3.0.0, available at: [https://earth.esa.int/documents/247904/2474726/Sentinel-5P-Level-2-Product-User-Manual-Nitrogen-Dioxide,\(last](https://earth.esa.int/documents/247904/2474726/Sentinel-5P-Level-2-Product-User-Manual-Nitrogen-Dioxide,(last)

access: 27 March 2019), 2018.

- Flagan, R. C. and Seinfeld, J. H.: Fundamentals of Air Pollution Engineering., Prentice-Hall, Inc., Englewood Cliffs, NJ, ISBN 0-13-332537-7, available at: <http://resolver.caltech.edu/CaltechBOOK:1988.001> (last access: 23 January 2019), 1988.
- van Geffen, J. H. G. M., Eskes, H. J., Boersma, K. F., Maasakkers, J. D. and Veefkind, J. P.: TROPOMI ATBD of the total and tropospheric NO₂ data products, S5P-KNMI-L2-0005-RP, issue 1.4.0, 6 February 2019, S5P-Knmi-L2-0005-Rp, (1.4.0), 1–76 [online] Available from: <https://sentinel.esa.int/documents/247904/2476257/Sentinel-5P-TROPOMI-ATBD-NO2-data-products>, 2019.
- Georgoulias, A. K., Van Der, R. A. J., Stammes, P., Folkert Boersma, K. and Eskes, H. J.: Trends and trend reversal detection in 2 decades of tropospheric NO₂ satellite observations, *Atmos. Chem. Phys.*, 19(9), 6269–6294, doi:10.5194/acp-19-6269-2019, 2019.
- van der Gon, H. D., Hendriks, C., Kuenen, J., Segers, A. and Visschedijk, A.: TNO Report: Description of current temporal emission patterns and sensitivity of predicted AQ for temporal emission patterns, Tech. rep., (December), 1–22, 2011.
- de Gouw, J. A., Parrish, D. D., Brown, S. S., Edwards, P., Gilman, J. B., Graus, M., Hanisco, T. F., Kaiser, J., Keutsch, F. N., Kim, S.-W., Lerner, B. M., Neuman, J. A., Nowak, J. B., Pollack, I. B., Roberts, J. M., Ryerson, T. B., Veres, P. R., Warneke, C. and Wolfe, G. M.: Hydrocarbon Removal in Power Plant Plumes Shows Nitrogen Oxide Dependence of Hydroxyl Radicals, *Geophys. Res. Lett.*, 0–2, doi:10.1029/2019GL083044, 2019.
- Grell, G. A., Peckham, S. E., Schmitz, R., McKeen, S. A., Frost, G., Skamarock, W. C. and Eder, B.: Fully coupled “online” chemistry within the WRF model, *Atmos. Environ.*, 39(37), 6957–6975, doi:10.1016/j.atmosenv.2005.04.027, 2005.
- Hong, S. and Lim, J.: HongandLim_JKMS_WSM6_2006, *J. Korean Meteorol. Soc.*, 42(2), 129–151 [online] Available from: http://www.mmm.ucar.edu/wrf/users/docs/WSM6-hong_and_lim_JKMS.pdf http://search.koreanstudies.net/journal/thesis_name.asp?tname=kiss2002&key=2525908, 2006.
- Hu, X. M., Klein, P. M. and Xue, M.: Evaluation of the updated YSU planetary boundary layer scheme within WRF for wind resource and air quality assessments, *J. Geophys. Res. Atmos.*, 118(18), 10,490–10,505, doi:10.1002/jgrd.50823, 2013.
- Huijnen, V., Pozzer, A., Arteta, J., Brasseur, G., Bouarar, I., Chabrilat, S., Christophe, Y., Doumbia, T., Flemming, J., Guth, J., Josse, B., Karydis, V. A., Marécal, V. and Pelletier, S.: Quantifying uncertainties due to chemistry modelling - Evaluation of tropospheric composition simulations in the CAMS model (cycle 43R1), *Geosci. Model Dev.*, 12(4), 1725–1752, doi:10.5194/gmd-12-1725-2019, 2019.
- Ialongo, I., Virta, H., Eskes, H., Hovila, J. and Douros, J.: Comparison of TROPOMI/Sentinel-5 Precursor NO₂ observations with ground-based measurements in Helsinki, *Atmos. Meas. Tech.*, 13(1), 205–218, doi:10.5194/amt-13-205-2020, 2020.

- Inness, A., Ades, M., Agustí-Panareda, A., Barr, J., Benedictow, A., Blechschmidt, A. M., Jose Dominguez, J., Engelen, R., Eskes, H., Flemming, J., Huijnen, V., Jones, L., Kipling, Z., Massart, S., Parrington, M., Peuch, V. H., Razinger, M., Remy, S., Schulz, M. and Suttie, M.: The CAMS reanalysis of atmospheric composition, *Atmos. Chem. Phys.*, 19(6), 3515–3556, doi:10.5194/acp-19-3515-2019, 2019.
- Krol, M., Houweling, S., Bregman, B., Broek, M. Van Den, Segers, A., Velthoven, P. Van, Peters, W. and Dentener, F.: and Physics The two-way nested global chemistry-transport zoom model TM5 : algorithm and applications, *Atmos. Chem. Phys.*, 417–432, <https://doi.org/10.5194/acp-5-417-2005>, 2005.
- Lama, S., Houweling, S., Folkert Boersma, K., Eskes, H., Aben, I., A. C. Denier Van Der Gon, H., C. Krol, M., Dolman, H., Borsdorff, T. and Lorente, A.: Quantifying burning efficiency in megacities using the NO₂•CO ratio from the Tropospheric Monitoring Instrument (TROPOMI), *Atmos. Chem. Phys.*, 20(17), 10295–10310, doi:10.5194/acp-20-10295-2020, 2020.
- Lambert, J.-C., A. Keppens, D. Hubert, B. Langerock, K.-U. Eichmann, Q. Kleipool, M. Snee, T. Verhoelst, T. Wagner, M. Weber, C. Ahn, A. Argyrouli, D. Balis, K.L. Chan, S. Compernelle, I. De Smedt, H. Eskes, A.M. Fjærraa, K. Garane, J.F. Gleason, F. Gouta, and P. W.: Sentinel-5 Precursor Mission Performance Centre Quarterly Validation Report of the Copernicus Sentinel-5 Precursor Operational Data Products, Issue # 03: Version 03.0.1, 125 pp., available at: https://www.tropomi.eu/sites/default/files/files/publicS5P-MPC-IASB-ROCVR-03.0.1-20190621_FINAL.pdf, (last access: 18 August 2019) , 2019.
- Lamsal, L. N., Martin, R. V., Van Donkelaar, A., Celarier, E. A., Bucsela, E. J., Boersma, K. F., Dirksen, R., Luo, C. and Wang, Y.: Indirect validation of tropospheric nitrogen dioxide retrieved from the OMI satellite instrument: Insight into the seasonal variation of nitrogen oxides at northern midlatitudes, *J. Geophys. Res. Atmos.*, 115(5), 1–15, doi:10.1029/2009JD013351, 2010.
- Landgraf, J., Aan De Brugh, J., Scheepmaker, R., Borsdorff, T., Hu, H., Houweling, S., Butz, A., Aben, I. and Hasekamp, O.: Carbon monoxide total column retrievals from TROPOMI shortwave infrared measurements, *Atmos. Meas. Tech.*, 9(10), 4955–4975, doi:10.5194/amt-9-4955-2016, 2016.
- Lang, M. N., Gohm, A. and Wagner, J. S.: The impact of embedded valleys on daytime pollution transport over a mountain range, *Atmos. Chem. Phys.*, doi:10.5194/acp-15-11981-2015, 2015.
- Lange, K., Richter, A. and Burrows, J. P.: Variability of nitrogen oxide emission fluxes and lifetimes estimated from Sentinel-5P TROPOMI observations, *Atmos. Chem. Phys. Discuss.*, 2(2), 1–32, doi:10.5194/acp-2021-273, 2021.
- Liu, F., Beirle, S., Zhang, Q., Dörner, S., He, K. and Wagner, T.: NO_x lifetimes and emissions of cities and power plants in polluted background estimated by satellite observations, *Atmos. Chem. Phys.*, 16(8), 5283–5298, doi:10.5194/acp-16-5283-2016, 2016.
- Lorente, A., Folkert Boersma, K., Yu, H., Dörner, S., Hilboll, A., Richter, A., Liu, M., Lamsal, L. N., Barkley, M., De Smedt,

- I., Van Roozendaal, M., Wang, Y., Wagner, T., Beirle, S., Lin, J. T., Krotkov, N., Stammes, P., Wang, P., Eskes, H. J. and
640 Krol, M.: Structural uncertainty in air mass factor calculation for NO₂ and HCHO satellite retrievals, *Atmos. Meas. Tech.*,
10(3), 759–782, doi:10.5194/amt-10-759-2017, 2017.
- Lorente, A., Boersma, K. F., Eskes, H. J., Veefkind, J. P., van Geffen, J. H. G. M., de Zeeuw, M. B., Denier van der Gon, H.
A. C., Beirle, S. and Krol, M. C.: Quantification of nitrogen oxides emissions from build-up of pollution over Paris with
TROPOMI, *Sci. Rep.*, 9(1), 1–10, doi:10.1038/s41598-019-56428-5, 2019a.
- 645 Lorente, A., Boersma, K. F., Eskes, H. J., Veefkind, J. P., van Geffen, J. H. G. M., de Zeeuw, M. B., Denier van der Gon, H.
A. C., Beirle, S. and Krol, M. C.: Quantification of nitrogen oxides emissions from build-up of pollution over Paris with
TROPOMI, *Sci. Rep.*, doi:10.1038/s41598-019-56428-5, 2019b.
- Lu, K. D., Hofzumahaus, A., Holland, F., Bohn, B., Brauers, T., Fuchs, H., Hu, M., Häseler, R., Kita, K., Kondo, Y., Li, X.,
Lou, S. R., Oebel, A., Shao, M., Zeng, L. M., Wahner, A., Zhu, T., Zhang, Y. H. and Rohrer, F.: Missing OH source in a
650 suburban environment near Beijing: Observed and modelled OH and HO₂ concentrations in summer 2006, *Atmos. Chem.*
Phys., 13(2), 1057–1080, doi:10.5194/acp-13-1057-2013, 2013.
- Tewari, M., Chen, F., Wang, W., Dudhia, J., LeMone, M. A., Mitchell, K., Ek, M., Gayno, G., Wegiel, J., and Cuenca, R. H.:
Implementation and verification of the unified Noah land surface model in the WRF model, in: the Conference on Weather
Analysis and Forecasting 11–15 January 2004, 1–6, Seattle, 2004.
- 655 MacIntyre, H. L. and Evans, M. J.: Sensitivity of a global model to the uptake of N₂O₅ by tropospheric aerosol, *Atmos. Chem.*
Phys., 10(15), 7409–7414, doi:10.5194/acp-10-7409-2010, 2010.
- Mlawer, E. J., Taubman, S. J., Brown, P. D., Iacono, M. J. and Clough, S. A.: Radiative transfer for inhomogeneous
atmospheres: RRTM, a validated correlated-k model for the longwave, *J. Geophys. Res. Atmos.*, 102(14), 16663–16682,
doi:10.1029/97jd00237, 1997.
- 660 Monks, P. S., Granier, C., Fuzzi, S., Stohl, A., Williams, M. L., Akimoto, H., Amann, M., Baklanov, A., Baltensperger, U.,
Bey, I., Blake, N., Blake, R. S., Carslaw, K., Cooper, O. R., Dentener, F., Fowler, D., Fragkou, E., Frost, G. J., Generoso, S.,
Ginoux, P., Grewe, V., Guenther, A., Hansson, H. C., Henne, S., Hjorth, J., Hofzumahaus, A., Huntrieser, H., Isaksen, I. S.
A., Jenkin, M. E., Kaiser, J., Kanakidou, M., Klimont, Z., Kulmala, M., Laj, P., Lawrence, M. G., Lee, J. D., Liousse, C.,
Maione, M., McFiggans, G., Metzger, A., Mieville, A., Moussiopoulos, N., Orlando, J. J., O’Dowd, C. D., Palmer, P. I.,
665 Parrish, D. D., Petzold, A., Platt, U., Pöschl, U., Prévôt, A. S. H., Reeves, C. E., Reimann, S., Rudich, Y., Sellegri, K.,
Steinbrecher, R., Simpson, D., ten Brink, H., Theloke, J., van der Werf, G. R., Vautard, R., Vestreng, V., Vlachokostas, C. and
von Glasow, R.: Atmospheric composition change - global and regional air quality, *Atmos. Environ.*, 43(33), 5268–5350,
doi:10.1016/j.atmosenv.2009.08.021, 2009.
- Moxim, W. J.: Simulated global tropospheric PAN: Its transport and impact on NO_x, *J. Geophys. Res. Atmos.*, 101(D7),

670 12621–12638, doi:10.1029/96JD00338, 1996.

Pascal, M., Corso, M., Chanel, O., Declercq, C., Badaloni, C., Cesaroni, G., Henschel, S., Meister, K., Haluza, D., Martin-Olmedo, P. and Medina, S.: Assessing the public health impacts of urban air pollution in 25 European cities: Results of the Aphekom project, *Sci. Total Environ.*, 449(2007105), 390–400, doi:10.1016/j.scitotenv.2013.01.077, 2013.

675 Pommier, M., McLinden, C. A. and Deeter, M.: Relative changes in CO emissions over megacities based on observations from space, *Geophys. Res. Lett.*, 40(14), 3766–3771, doi:10.1002/grl.50704, 2013.

Romer, P. S., Duffey, K. C., Wooldridge, P. J., Edgerton, E., Baumann, K., Feiner, P. A., Miller, D. O., Brune, W. H., Koss, A. R., De Gouw, J. A., Misztal, P. K., Goldstein, A. H. and Cohen, R. C.: Effects of temperature-dependent NO_x emissions on continental ozone production, *Atmos. Chem. Phys.*, doi:10.5194/acp-18-2601-2018, 2018.

680 Romer Present, P. S., Zare, A. and Cohen, R. C.: The changing role of organic nitrates in the removal and transport of NO_x, *Atmos. Chem. Phys. Discuss.*, (x), 1–18, doi:10.5194/acp-2019-471, 2019.

Sannigrahi, S., Kumar, P., Molter, A., Zhang, Q., Basu, B., Basu, A. S. and Pilla, F.: Examining the status of improved air quality in world cities due to COVID-19 led temporary reduction in anthropogenic emissions, *Environ. Res.*, 196(September 2020), 110927, doi:10.1016/j.envres.2021.110927, 2021.

685 Shah, V., J. Jacob, D., Li, K., Silvern, R., Zhai, S., Liu, M., Lin, J. and Zhang, Q.: Effect of changing NO_x lifetime on the seasonality and long-term trends of satellite-observed tropospheric NO₂ columns over China, *Atmos. Chem. Phys.*, 20(3), 1483–1495, doi:10.5194/acp-20-1483-2020, 2020.

Sicard, P., Agathokleous, E., De Marco, A., Paoletti, E. and Calatayud, V.: Urban population exposure to air pollution in Europe over the last decades, *Environ. Sci. Eur.*, 33(1), doi:10.1186/s12302-020-00450-2, 2021.

690 Sobanski, N., Thieser, J., Schuladen, J., Sauvage, C., Song, W., Williams, J., Lelieveld, J. and Crowley, J. N.: Day and night-time formation of organic nitrates at a forested mountain site in south-west Germany, *Atmos. Chem. Phys.*, doi:10.5194/acp-17-4115-2017, 2017.

Stavrakou, T., Müller, J. F., Boersma, K. F., Van Der A., R. J., Kurokawa, J., Ohara, T. and Zhang, Q.: Key chemical NO_x sink uncertainties and how they influence top-down emissions of nitrogen oxides, *Atmos. Chem. Phys.*, 13(17), 9057–9082, doi:10.5194/acp-13-9057-2013, 2013.

695 United Nations: World Urbanization Prospects : an alternative to the UN model of projection compatible with the mobility transition theory, *Demogr. Res.*, 12, 197–236, <https://doi.org/10.4054/demres.2005.12.9>, 2018.

Valin, L. C., Russell, A. R., Hudman, R. C. and Cohen, R. C.: Effects of model resolution on the interpretation of satellite NO₂ observations, *Atmos. Chem. Phys.*, 11(22), 11647–11655, doi:10.5194/acp-11-11647-2011, 2011.

Valin, L. C., Russell, A. R. and Cohen, R. C.: Variations of OH radical in an urban plume inferred from NO₂ column

- 700 measurements, *Geophys. Res. Lett.*, doi:10.1002/grl.50267, 2013.
- Veefkind, J. P., Aben, I., McMullan, K., Förster, H., de Vries, J., Otter, G., Claas, J., Eskes, H. J., de Haan, J. F., Kleipool, Q., van Weele, M., Hasekamp, O., Hoogeveen, R., Landgraf, J., Snel, R., Tol, P., Ingmann, P., Voors, R., Kruizinga, B., Vink, R., Visser, H. and Levelt, P. F.: TROPOMI on the ESA Sentinel-5 Precursor: A GMES mission for global observations of the atmospheric composition for climate, air quality and ozone layer applications, *Remote Sens. Environ.*, doi:10.1016/j.rse.2011.09.027, 2012.
- 705 Verstraeten, W. W., Boersma, K. F., Douros, J., Williams, J. E., Eskes, H., Liu, F., Beirle, S. and Delcloo, A.: Top-down NO_x emissions of european cities based on the downwind plume of modelled and space-borne tropospheric NO₂ columns, *Sensors (Switzerland)*, 18(9), doi:10.3390/s18092893, 2018.
- Visser, A. J., Folkert Boersma, K., Ganzeveld, L. N. and Krol, M. C.: European NO_x emissions in WRF-Chem derived from
710 OMI: Impacts on summertime surface ozone, *Atmos. Chem. Phys.*, 19(18), 11821–11841, doi:10.5194/acp-19-11821-2019, 2019.
- Wennberg, P. O., Stremme, W., Schneider, M., Feist, D. G., aan de Brugh, J., Toon, G. C., De Mazière, M., Gross, J., Grutter, M., Hu, H., Rettinger, M., Roehl, C., Pollard, D. F., Hasekamp, O., Hase, F., Borsdorff, T., Garcia, O., Kumar Sha, M., Arnold, S. G., Landgraf, J., Sussmann, R. and Kiel, M.: Mapping carbon monoxide pollution from space down to city scales with daily
715 global coverage, *Atmos. Meas. Tech.*, 11(10), 5507–5518, doi:10.5194/amt-11-5507-2018, 2018.
- Zhang, C. and Wang, Y.: Projected future changes of tropical cyclone activity over the Western North and South Pacific in a 20-km-Mesh regional climate model, *J. Clim.*, 30(15), 5923–5941, doi:10.1175/JCLI-D-16-0597.1, 2017.